



**Defect formation and carrier compensation in the layered  
oxychalcogenide  $\text{La}_2\text{CdO}_2\text{Se}_2$ : an insight from first  
principles**

Journal:	<i>Journal of Materials Chemistry C</i>
Manuscript ID	TC-ART-09-2022-003836.R1
Article Type:	Paper
Date Submitted by the Author:	10-Oct-2022
Complete List of Authors:	Gake, Tomoya; Tokyo Institute of Technology, Laboratory for Materials and Structures Kumagai, Yu; Tokyo Institute of Technology, Laboratory for Materials and Structures Takahashi, Akira; Tokyo Institute of Technology, Laboratory for Materials and Structures Hiramatsu, Hidenori; Tokyo Institute of Technology, Laboratory for Materials and Structures Oba, Fumiyasu ; Tokyo Institute of Technology, Laboratory for Materials and Structures

Cite this: DOI: 00.0000/xxxxxxxxxx

## Defect formation and carrier compensation in the layered oxychalcogenide $\text{La}_2\text{CdO}_2\text{Se}_2$ : an insight from first principles<sup>†</sup>

Tomoya Gake, Yu Kumagai, Akira Takahashi, Hidenori Hiramatsu, and Fumiyasu Oba\*

Received Date

Accepted Date

DOI: 00.0000/xxxxxxxxxx

The layered oxychalcogenide  $\text{La}_2\text{CdO}_2\text{Se}_2$  is a candidate for an n-type transparent conductive material, but electrical insulating properties have hitherto been reported for both undoped and donor-doped  $\text{La}_2\text{CdO}_2\text{Se}_2$ . In this study, we investigate native defects and extrinsic dopants in  $\text{La}_2\text{CdO}_2\text{Se}_2$  using first-principles calculations based on the Heyd-Scuseria-Ernzerhof hybrid functional approach. The calculated band structure and effective masses show two-dimensional characteristics, reflecting the layered structure. The energetics of the native defects indicates that negatively charged Cd vacancies and positively charged Cd interstitials are dominant at high and low Fermi level positions, respectively. The balance of these defects associated with Cd deficiency and excess leads the equilibrium Fermi level to a mid-gap position, which explains the experimentally reported nearly stoichiometric and electrical insulating behavior of undoped  $\text{La}_2\text{CdO}_2\text{Se}_2$ . Among various dopants selected from group-I to IV elements, Al at the Cd site forms a shallow donor level, and Sr at the La site forms a shallow acceptor level. However, the carriers generated by these dopants are severely compensated by the native defects charged with the opposite sign, in consistency with the reported insulating properties of donor-doped  $\text{La}_2\text{CdO}_2\text{Se}_2$ . It is suggested that  $\text{La}_2\text{CdO}_2\text{Se}_2$  is prone to form the Cd vacancies and interstitials compared to zincblende-CdSe, which has a similar local structure to the selenide layer in  $\text{La}_2\text{CdO}_2\text{Se}_2$ , partly because of a flexible structural relaxation related to its two-dimensional crystal structure. Such a detailed understanding of the defect properties in the non-Cu-based oxychalcogenide  $\text{La}_2\text{CdO}_2\text{Se}_2$  is meaningful for further developing design principles for transparent conductive materials.

### 1 Introduction

Transparent conductive oxides (TCOs) are essential electrode materials for display, solar cells, and so forth.<sup>1,2</sup> Reflecting the typical electronic structure of oxides, most TCOs exhibit n-type conductivity as exemplified by donor-doped  $\text{In}_2\text{O}_3$ ,<sup>3–5</sup>  $\text{SnO}_2$ ,<sup>6–8</sup> and  $\text{ZnO}$ ,<sup>9,10</sup> and only a limited number of TCOs exhibit p-type conductivity. A prototypical p-type TCO is  $\text{CuAlO}_2$ , as reported by Kawazoe *et al.*<sup>11</sup> They had an eye to the  $d^{10}$  electronic configuration of  $\text{Cu}^+$  and proposed that the Cu 3d-orbitals hybridize with the O 2p-orbitals near the top of the VB, resulting in a higher VB position than those of typical oxides and thus facilitating hole doping. Starting with the proposal of this strategy, compounds containing a cation with  $d^{10}$  or  $s^2$  electronic configurations<sup>11–15</sup> and/or containing an anion other than O<sup>16–18</sup> have attracted attention, and several candidates of p-type TCOs, or more generally,

transparent conductive materials (TCMs), have been found.<sup>19,20</sup> One of them is  $\text{LaCuOS}$ ,<sup>16</sup> an oxychalcogenide with a layered structure consisting of alternating oxide ( $[\text{La}_2\text{O}_2]^{2+}$ ) and sulfide ( $[\text{Cu}_2\text{S}_2]^{2-}$ ) layers.  $\text{LaCuOS}$  has a wide band gap (3.1 eV<sup>16</sup>) derived from the oxide nature, a large VB dispersion derived from the sulfide nature, and a high VB position. It has been reported that a high carrier concentration of  $10^{20} \text{ cm}^{-3}$  can be obtained by heavy Mg doping, but the mobility is as low as  $\sim 0.2 \text{ cm}^2 \text{ V}^{-1} \text{ s}^{-1}$ , and the electrical conductivity is as low as  $\sim 5 \text{ S cm}^{-1}$ .<sup>21</sup> Interestingly, the mobility and electrical conductivity of  $\text{LaCuOS}$  increase monotonically by substituting S with Se.<sup>17,21</sup> The heavy Mg doping into  $\text{LaCuOSe}$ , in which S is fully replaced by Se, can achieve the mobility of  $3.5 \text{ cm}^2 \text{ V}^{-1} \text{ s}^{-1}$  and the electrical conductivity of  $910 \text{ S cm}^{-1}$  at the carrier concentration of  $10^{21} \text{ cm}^{-3}$ .<sup>18</sup> However, the optical band gap of  $\text{LaCuOSe}$  of 2.8 eV<sup>22</sup> is in the visible light range, and a wider gap is ideal as a transparent conductor. p-Type TCMs with both high conductivity (in the order of  $10^4 \text{ S cm}^{-1}$ ) and wide optical band gaps comparable to practically used n-type TCMs such as  $\text{In}_2\text{O}_3:\text{Sn}$  and  $\text{SnO}_2:\text{F}$  have not yet been found.

In addition to the aforementioned features, layered oxychalco-

Laboratory for Materials and Structures, Institute of Innovative Research, Tokyo Institute of Technology, Yokohama 226-8503, Japan. E-mail: oba@msl.titech.ac.jp

<sup>†</sup> Electronic Supplementary Information (ESI) available. See DOI: 00.0000/00000000.

genides have two-dimensional crystal structures, which can be advantageous for carrier doping compared to typical three-dimensional oxides and chalcogenides.<sup>21,23</sup> When carrier concentration is increased by heavy doping in typical semiconductors, carrier scattering by the dopant becomes pronounced, resulting in a significant decrease in mobility. However, in layered oxychalcogenides with two-dimensional structures consisting of alternating oxide and chalcogenide layers such as  $\text{LaCuOCh}$  ( $Ch = \text{S, Se}$ ), the latter layer is mainly responsible for hole conduction. Hence, if dopants that can easily enter the oxide layer are selected, the hole-generating layer containing dopants and the hole-conducting layer can be spatially separated. This spatial separation makes it possible to simultaneously achieve high carrier concentration and relatively high mobility.<sup>21</sup> In fact, doped  $\text{LaCuOCh}$  shows a decrease in mobility to only about half the values of undoped samples.<sup>21</sup>

The applications of TCMs as semiconductors in electronic and optoelectronic devices have also attracted tremendous interest.<sup>1</sup> In order to create high-efficiency semiconductor devices while taking advantage of the structural benefits of oxychalcogenides, either carrier type conversion into n-type or another n-type semiconductor with a similar structure is needed to avoid a large mismatch in the lattice and atomic structure when creating a pn junction. However, n-type  $\text{LaCuOCh}$  has not been realized. The theoretical study by Scanlon *et al.* has shown that carrier electrons are easily compensated by negatively charged Cu vacancies in  $\text{LaCuOSe}$ .<sup>24</sup>

From this circumstance, Hiramatsu *et al.* focused on the layered oxychalcogenide  $\text{La}_2\text{CdO}_2\text{Se}_2$ , which has a similar structure to  $\text{LaCuOCh}$  but does not contain Cu, and investigated its optical and electrical properties.<sup>25,26</sup> They reported that  $\text{La}_2\text{CdO}_2\text{Se}_2$  has an optical band gap of 3.3 eV, which is in the UV region, but their samples exhibit electrical insulating properties even with Al or Zr donor doping. It is not clear whether the lack of n-type conductivity is due to the intrinsic behavior of these dopants or the carrier compensation by native defects. Furthermore,  $\text{La}_2\text{CdO}_2\text{Se}_2$  also has the potential to be a p-type TCM because its valence band maximum (VBM) is mainly formed from the Se 4p-orbitals, which have higher orbital energy than that of the O 2p-orbitals. However, its p-type dopability has not been well investigated both experimentally and theoretically. A detailed understanding of the behavior of the native defects and dopants in the non-Cu-based oxychalcogenide  $\text{La}_2\text{CdO}_2\text{Se}_2$ , as well as Cu-based systems,<sup>24,27–29</sup> is meaningful for further developing design principles for p-type TCMs and related materials.<sup>20,30,31</sup>

In this study, the carrier generation and compensation by native defects and extrinsic dopants in  $\text{La}_2\text{CdO}_2\text{Se}_2$  are examined using first-principles calculations based on a hybrid functional approach. First, the bulk properties of  $\text{La}_2\text{CdO}_2\text{Se}_2$  are investigated and compared to zincblende-CdSe (zb-CdSe), which has a similar local structure to the selenide layer in  $\text{La}_2\text{CdO}_2\text{Se}_2$ . Next, we identify which native defects are associated with carrier generation and compensation in terms of their formation energies and acceptor/donor behavior. Our investigation is then extended to Na, Sr, Al, and Zr dopants selected via computational screening of group-I to IV elements based on their acceptor/donor levels and

formation energies. Finally, the doping limit determined by the carrier compensation due to the formation of the native defects is discussed by comparing  $\text{La}_2\text{CdO}_2\text{Se}_2$  with zb-CdSe.

## 2 Computational details

The first-principles calculations were performed using the projector augmented-wave (PAW) method<sup>32</sup> as implemented in the VASP code.<sup>33–35</sup> For the exchange-correlation functional, we used the Heyd-Scuseria-Ernzerhof (HSE06) hybrid functional,<sup>36,37</sup> which includes a Fock exchange parameter of 0.25 and a screening parameter of  $0.21 \text{ \AA}^{-1}$ . The PAW radial cutoffs were set to 1.48, 1.22, 0.80, 1.11, 1.16, 1.32, 1.01, and  $1.32 \text{ \AA}$  for La, Cd, O, Se, Na, Sr, Al, and Zr, respectively. La 5s, 5p, 6s, and 5d, Cd 4d and 5s, O 2s and 2p, Se 4s and 4p, Na 3s, Sr 4s, 4p, and 5s, Al 3s and 3p, and Zr 4s, 4p, 5s, and 4d were treated as valence electrons. The lattice constants and internal atomic coordinates of the primitive unit cell were relaxed until the residual stresses and atomic forces converged to 0.022 GPa and  $0.005 \text{ eV \AA}^{-1}$ . A  $5 \times 5 \times 2$  non- $\Gamma$ -centered k-point mesh and a plane-wave cutoff energy of 520 eV were used for the structural optimization. The band structure and density of states (DOS) were evaluated using a cutoff energy of 400 eV under the optimized structure. The band path was determined using the seekpath code,<sup>38</sup> which relies on the symmetry search using the spglib code.<sup>39</sup> For the DOS calculation, a  $10 \times 10 \times 4$   $\Gamma$ -centered k-point mesh was employed with a reduced mesh by a factor of 2 for the Fock exchange potential. The band-averaged effective mass tensor was calculated using the BoltzTraP2 code,<sup>40</sup> where the carrier concentration and temperature were set to  $10^{16} \text{ cm}^{-3}$  and 300 K, respectively, and a  $\Gamma$ -centered k-point mesh of  $20 \times 20 \times 8$  was taken with a reduced mesh by a factor of 4 for the Fock exchange potential. The input files for the VASP calculations were generated by the vise code.<sup>41</sup>

For the defect calculations, the vacancies ( $V_{\text{La}}, V_{\text{Cd}}, V_{\text{O}}, V_{\text{Se}}$ ), the cation antisites ( $\text{La}_{\text{Cd}}, \text{Cd}_{\text{La}}$ ), and the interstitials ( $\text{La}_i, \text{Cd}_i, \text{O}_i, \text{Se}_i$ ) were considered as the native defects, and extrinsic dopants on the cation sites ( $\text{Na}_{\text{Cd}}, \text{Sr}_{\text{La}}, \text{Al}_{\text{Cd}}, \text{Zr}_{\text{La}}$ ) and the interstitial sites ( $\text{Na}_i, \text{Sr}_i, \text{Al}_i, \text{Zr}_i$ ). Here, the type of defects is denoted by  $X_Y$ , where  $X$  is the vacancy ( $V$ ) or element and  $Y$  is the defect site ( $i$  is the interstitial site). The cation-anion antisites and anion-anion antisites were not taken into account. These defects were modeled using a 126-atom supercell that enlarged the primitive cell by a factor of  $3 \times 3 \times 1$ . The site with the smallest all-electron charge density in the perfect crystal was extracted using the pymatgen code<sup>42</sup> and adopted as the interstitial site [Fig. 1(a)]. The initial structure of each supercell was subjected to random displacements of up to  $0.2 \text{ \AA}$  for the atoms adjacent to the defects, eliminating symmetry-induced relaxation constraints. The internal atomic coordinates were relaxed under the fixed lattice constants until the atomic forces became smaller than  $0.03 \text{ eV \AA}^{-1}$ . A  $2 \times 2 \times 1$  non- $\Gamma$ -centered k-point mesh and a plane wave cutoff of 400 eV was used, and spin polarization was considered in all supercell calculations.

The formation energy of defect  $D$  in charge state  $q$  ( $E_{\text{f}}[D^q]$ ) is expressed as

$$E_f[D^q] = E[D^q] + E_{\text{corr}}[D^q] - E_p - \sum_i \Delta n_i \mu_i + q(\varepsilon_{\text{VBM}} + \Delta\varepsilon_F), \quad (1)$$

where  $E[D^q]$  and  $E_p$  are the total energies of the supercell containing defect  $D$  in charge state  $q$  and the perfect-crystal supercell, respectively.  $\Delta n_i$  is the difference in the number of the constituent  $i$ -type atoms between the defect and perfect-crystal supercells, and  $\mu_i$  is the chemical potential of the  $i$ -type atom.  $\Delta\varepsilon_F$  is the position of the Fermi level relative to the VBM ( $\varepsilon_{\text{VBM}}$ ).  $E_{\text{corr}}[D^q]$  is the correction term for  $E[D^q]$  due to spurious electrostatic interactions in finite-size supercells containing charged defects, for which the extended Freysoldt-Neugebauer-Van de Walle method<sup>43,44</sup> was applied.

The chemical potential diagrams of the La-Cd-O-Se quaternary system at 0 K and 0 Pa were calculated to determine the single-phase region of  $\text{La}_2\text{CdO}_2\text{Se}_2$ . The substances consisting of any one to four elements from La, Cd, O, and Se were selected from the Materials Project<sup>45</sup> using a criterion of energy above hull less than 0.05 meV atom<sup>-1</sup> and considered as the competing phases. For the  $\text{O}_2$  phase, a supercell containing an  $\text{O}_2$  molecule in a 10 Å cubic cell was used instead of modeling of a stable molecular crystal at 0 K and 0 Pa. The standard states were set to the La, Cu, and Se crystals and the  $\text{O}_2$  molecule. The same conditions and criteria were used for Na, Sr, Al, and Zr dopants, and the chemical potential diagrams were calculated for the quinary system. The standard states of the dopant elements were set to the Na, Sr, Al, and Zr crystals. Hereafter, the values of the chemical potentials will be expressed relative to those in the standard states ( $\Delta\mu_i$ ).

The static dielectric tensor ( $\varepsilon_0$ ) for describing the long-range electrostatic screening effect is expressed as the ion-clamped dielectric tensor, represented as the sum of the vacuum permittivity and the electronic contribution ( $\varepsilon^{\text{ele}}$ ), plus the ionic contribution ( $\varepsilon^{\text{ion}}$ ).  $\varepsilon_0$  was calculated by the finite-electric-field approach<sup>46</sup> using a  $10 \times 10 \times 4$  non- $\Gamma$ -centered k-point mesh and a cutoff energy of 400 eV, where the k-point mesh was reduced by a factor of 2 for the Fock exchange potential. The components of the obtained dielectric tensor were  $\varepsilon_{xx}^{\text{le}} = 5.61$ ,  $\varepsilon_{zz}^{\text{le}} = 5.30$ ,  $\varepsilon_{xx}^{\text{ion}} = 13.08$ , and  $\varepsilon_{zz}^{\text{ion}} = 7.68$ , which were used to calculate  $E_{\text{corr}}[D^q]$ . The differences in the corrected formation energies of the major native defects, namely  $V_{\text{Cd}}^{-2}$  and  $\text{Cd}_i^{+2}$ , in the supercells that enlarged the primitive cell by factors of  $3 \times 3 \times 1$  and  $4 \times 4 \times 1$  were only less than 0.06 eV. For handling and analyzing the defect calculations, the pydefect code<sup>41</sup> was used.

From Eq. 1, the thermodynamic transition levels between charge states  $q$  and  $q'$  ( $q > q'$ ) with respect to the VBM can be expressed as<sup>47,48</sup>

$$\varepsilon(q/q') = \frac{E_f[D^q, \Delta\varepsilon_F = 0] - E_f[D^{q'}, \Delta\varepsilon_F = 0]}{q' - q}, \quad (2)$$

where  $E_f[D^q, \Delta\varepsilon_F = 0]$  is the formation energy of  $D^q$  when the Fermi level is at the VBM. The thermodynamic transition level corresponds to the Fermi level position at which the energetically most stable defect charge state changes. Hence, when the Fermi level is lower than  $\varepsilon(q/q')$ , the defect takes charge state  $q$ ; when

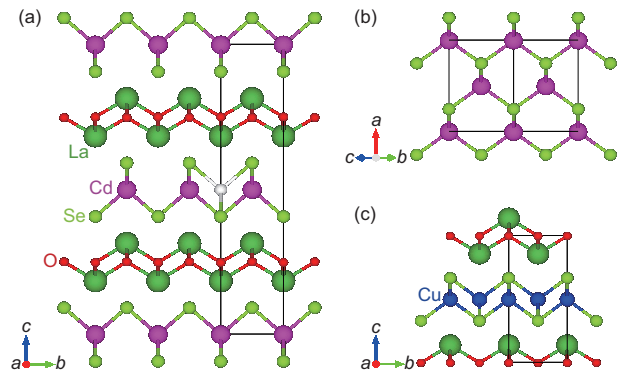


Fig. 1 (a) Crystal structure of  $\text{La}_2\text{CdO}_2\text{Se}_2$ . The interstitial site considered in the defect calculations is shown as the white sphere. Crystal structures of (b) zb-CdSe and (c) LaCuOSe. The frames indicate respective conventional unit cells.

it is higher than  $\varepsilon(q/q')$ , the defect takes charge state  $q'$ .  $\varepsilon(q/q')$  ( $q \leq 0$ ) measured from the VBM and  $\varepsilon(q/q')$  ( $q' \geq 0$ ) measured from the conduction band minimum (CBM) correspond to acceptor and donor levels, respectively.

## 3 Results and discussion

### 3.1 Bulk properties

Figure 1(a) shows the crystal structure of  $\text{La}_2\text{CdO}_2\text{Se}_2$  as reported experimentally.<sup>25</sup> It belongs to the tetragonal lattice system with the space group  $P4_2/nmc$  and has only one equivalent site for each element. The crystal structure of  $\text{La}_2\text{CdO}_2\text{Se}_2$  is characterized by a layered structure with alternating oxide ( $[\text{La}_2\text{O}_2]^{2+}$ ) and selenide layers ( $[\text{CdSe}_2]^{2-}$ ), and the latter has a local structure similar to the (100) stacking of zb-CdSe [Fig. 1(b)]. It is also similar to that of LaCuOSe [Fig. 1(c)],<sup>49</sup> and their structures match when half of the Cu atoms is periodically removed from LaCuOSe. Therefore, the structure of  $\text{La}_2\text{CdO}_2\text{Se}_2$  has a vacant site surrounded by four Se atoms as in the case of zb-CdSe. According to the analysis of the all-electron charge density, its minimum is situated at the vacant site. For this reason, we considered it as the interstitial site [Fig. 1(a)]. The theoretical lattice constants of  $\text{La}_2\text{CdO}_2\text{Se}_2$  are  $a = 4.07$  Å and  $c = 18.81$  Å, reproducing the experimental lattice constants of  $a = 4.0660$  Å and  $c = 18.634$  Å<sup>25</sup> within an error of 1%.

Figure 2(a) shows the band structure, the total DOS, and the DOS projected on each of the atomic site and orbital for  $\text{La}_2\text{CdO}_2\text{Se}_2$ .  $\text{La}_2\text{CdO}_2\text{Se}_2$  has a direct-type band structure with the VBM and CBM located at the  $\Gamma$  point, which is consistent with the previously reported theoretical band structure.<sup>26</sup> The calculated band gap of 3.03 eV is close to the experimental band gap of  $\sim 3.3$  eV.<sup>25,26</sup> Figure 2(b) shows the band structure and the DOSs for zb-CdSe (see the ESI† for computational details). The band gap of zb-CdSe is calculated to be 1.47 eV (1.7 eV by experiment<sup>50</sup>), which is much smaller than that of  $\text{La}_2\text{CdO}_2\text{Se}_2$ . The reason can be explained in terms of the differences of the crystal structures and the DOSs.<sup>26</sup> Looking at the DOS of  $\text{La}_2\text{CdO}_2\text{Se}_2$ , the VB has a bandwidth of  $\sim 5$  eV and its upper and lower parts are mainly formed from Se p-orbitals and O p-orbitals, respectively,

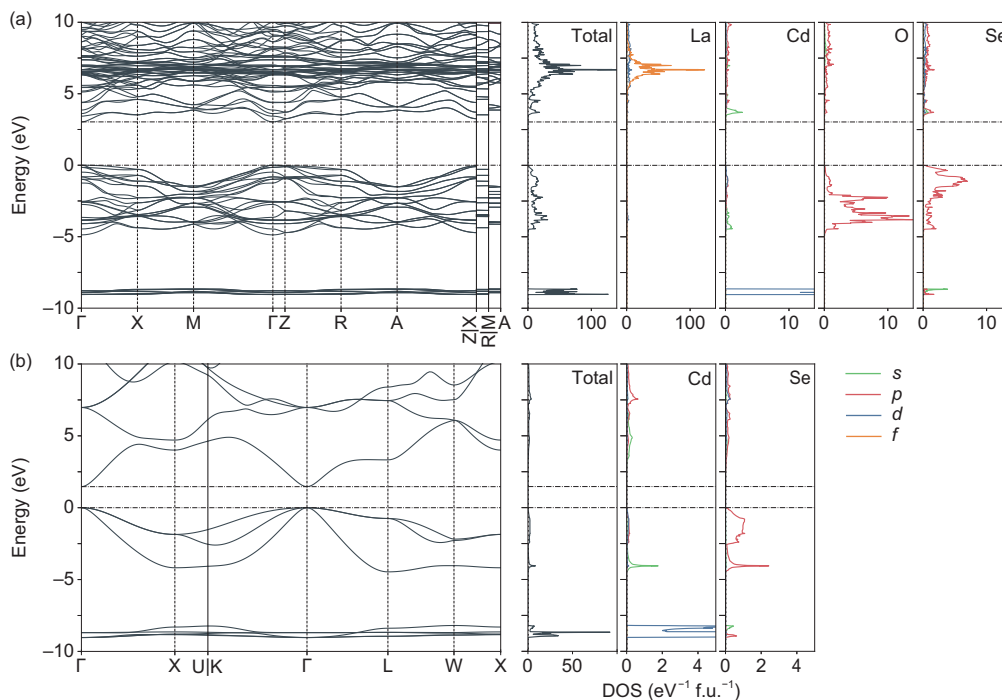


Fig. 2 Band structure, total DOS, and the DOS projected on the respective atomic sites and orbitals for (a)  $\text{La}_2\text{CdO}_2\text{Se}_2$  and (b)  $\text{zb-CdSe}$ . The energy zeros are set at the respective VBMs.

while the CBM is mainly formed from Cd s-orbitals and the La f-orbital components are located mainly at  $\sim 3$  eV above the CBM [Fig. 2(a)]. The band gap of  $\text{La}_2\text{CdO}_2\text{Se}_2$  is mainly determined by the selenide layer, as reported previously.<sup>26</sup> The upper VB is also formed by Se p-orbitals and the lower conduction band by Cd s-orbitals in  $\text{zb-CdSe}$  [Fig. 2(b)]. However, unlike  $\text{zb-CdSe}$ , the selenide layer that forms the VBM and CBM are spatially separated by the oxide layer in  $\text{La}_2\text{CdO}_2\text{Se}_2$ . This suggests that the inter-layer overlap of the Se-Se and Cd-Cd wave functions is weakened, resulting in a smaller band dispersion and a wider band gap.<sup>26</sup> The in-plane and out-of-plane band-averaged effective masses of  $\text{La}_2\text{CdO}_2\text{Se}_2$  are  $0.29m_0$  and  $0.40m_0$  for electrons and  $0.70m_0$  and  $3.74m_0$  for holes, respectively, where  $m_0$  is the free-electron rest mass, reflecting the two-dimensional crystal and electronic structures. The band structure also confirms that the band dispersion is smaller in the  $\Gamma$ -Z direction, corresponding to the out-of-plane direction [Fig. 2(a)]. The band-averaged effective masses of  $\text{zb-CdSe}$  are  $0.12m_0$  for electrons and  $0.74m_0$  for holes. The fact that the average effective masses of electrons and holes are larger in  $\text{La}_2\text{CdO}_2\text{Se}_2$  is consistent with the aforementioned explanation of the two-dimensional band structure. The average effective mass of electrons in  $\text{La}_2\text{CdO}_2\text{Se}_2$  is relatively smaller than the reported values of Cu-based wide-gap p-type oxide semiconductors such as  $\text{CuAlO}_2$  ( $0.89m_0$  on average) and  $\text{LaCuOSe}$  ( $1.17m_0$  on average), not much different from the typical n-type TCMs such as  $\text{In}_2\text{O}_3$  ( $0.17m_0$ ) and  $\text{SnO}_2$  ( $0.17m_0$  on average).<sup>51</sup> In addition, anisotropy in the electron effective mass is not significant despite the layered structure of  $\text{La}_2\text{CdO}_2\text{Se}_2$ . These features in the electron effective mass are attributed to the spatially-spread Cd s characteristic at the CBM. The effective mass of holes in the in-

plane direction is very small compared to  $\text{CuAlO}_2$  ( $1.92m_0$ ) and not much different from that of  $\text{LaCuOSe}$  ( $0.63m_0$ ), while in the out-of-plane direction it is considerably large as in the Cu-based ones ( $5.22m_0$  for  $\text{CuAlO}_2$  and  $2.83m_0$  for  $\text{LaCuOSe}$ ).<sup>51</sup>

### 3.2 Native defects

To discuss the energetics of the native defects under relevant chemical potential conditions, we calculated the chemical potential diagram for the La-Cd-O-Se quaternary system and found eight chemical potential limits where  $\text{La}_2\text{CdO}_2\text{Se}_2$  exists in the single phase. The values of the chemical potentials at each limit and the competing phases are shown in the ESI† [Table S1]. To obtain insight into the dopability of  $\text{La}_2\text{CdO}_2\text{Se}_2$ , two representative chemical potential limits are considered here: (i) the limit where the chemical potentials of La and Cd are maximized and those of O and Se are minimized [ $\Delta\mu_{\text{La}} = -3.45$ ,  $\Delta\mu_{\text{Cd}} = 0$ ,  $\Delta\mu_{\text{O}} = -4.07$ , and  $\Delta\mu_{\text{Se}} = -1.52$  (eV)] and (ii) the limit where the chemical potentials of La and Cd are minimized, and those of O and Se are maximized [ $\Delta\mu_{\text{La}} = -6.23$ ,  $\Delta\mu_{\text{Cd}} = -1.09$ ,  $\Delta\mu_{\text{O}} = -1.84$ , and  $\Delta\mu_{\text{Se}} = -0.42$  (eV)]. Hereafter, we refer to the former as the Cation-rich condition and the latter as the Anion-rich condition.

Figure 3(a) shows the formation energy diagram for the selected native defects in  $\text{La}_2\text{CdO}_2\text{Se}_2$  at the Cation-rich condition. The positions of the thermodynamic transition levels are listed in the ESI† [Table S2]. In terms of the chemical potential dependence, the formation energies of the donor-type defects ( $V_{\text{O}}$ ,  $V_{\text{Se}}$ ,  $\text{La}_{\text{Cd}}$ ,  $\text{La}_i$ , and  $\text{Cd}_i$ ) are minimized at this condition. However, their formation energies are generally high when the Fermi level is close to the CBM. Moreover, all of these defects form only

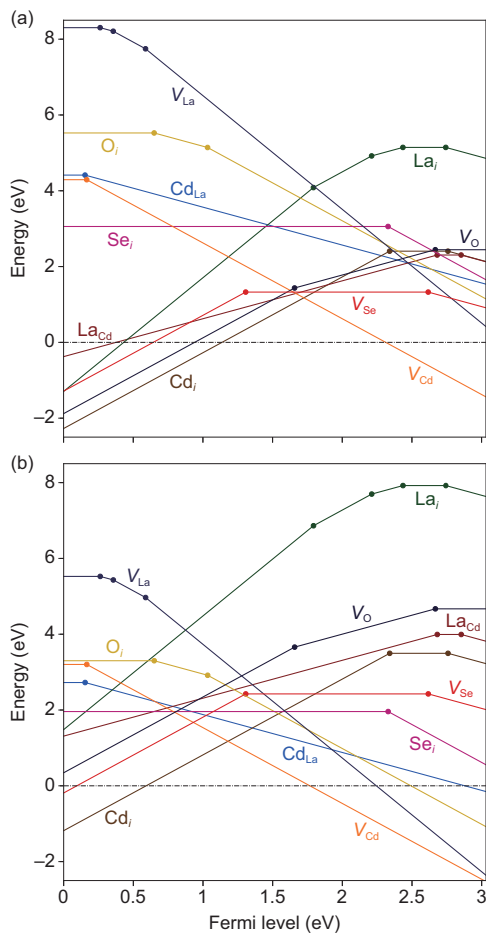


Fig. 3 Formation energies of native defects in  $\text{La}_2\text{CdO}_2\text{Se}_2$  at (a) Cation-rich and (b) Anion-rich conditions. The type of defect is indicated by  $X_Y$ , where  $X$  is the vacancy ( $V$ ) or element and  $Y$  is the defect site ( $i$  is the interstitial site). The range of the Fermi level is given by the VBM (set to zero) and the CBM. For each defect, the formation energy in the most stable charge state at a Fermi level position is plotted, and the slope of the line corresponds to the defect charge state. The thermodynamic transition levels, corresponding to the positions of the Fermi level at which the energetically preferred defect charge states change, are indicated by filled circles. The positions of the thermodynamic transition levels are listed in Table S2.

deep levels, indicating that they cannot be major sources of carrier electrons. In particular, the formation energy of  $V_{\text{Se}}$  is relatively low among these defects, but its donor level [ $\epsilon(+2/0)$ ] is located at  $-1.72$  eV from the CBM. In addition, although  $V_{\text{Se}}$ ,  $\text{La}_{\text{Cd}}$ ,  $\text{La}_i$ , and  $\text{Cd}_i$  are formally donor-type defects, the  $-1$  charge state is stable when the Fermi level is close to the CBM, suggesting that they rather act to compensate carrier electrons. Among the acceptor-type defects ( $V_{\text{Cd}}$ ,  $V_{\text{La}}$ ,  $\text{Cd}_{\text{La}}$ ,  $\text{O}_i$ , and  $\text{Se}_i$ ),  $V_{\text{Cd}}$  shows an exceedingly low formation energy at high Fermi level positions. Although the formation energy of  $V_{\text{Cd}}^{-2}$  is highest at the Cation-rich condition in terms of the chemical potential dependence, it is negative when the Fermi level is above 2.31 eV. Therefore, carrier electrons generated by native and extrinsic donors are expected to be strongly compensated by  $V_{\text{Cd}}^{-2}$ .

Figure 3(b) shows the formation energy diagram for the selected native defects in  $\text{La}_2\text{CdO}_2\text{Se}_2$  at the Anion-rich condition.

The formation energies of the acceptor-type defects ( $V_{\text{Cd}}$ ,  $V_{\text{La}}$ ,  $\text{Cd}_{\text{La}}$ ,  $\text{O}_i$ , and  $\text{Se}_i$ ) are minimized at this condition, but the formation energies are generally high when the Fermi level is close to the VBM.  $V_{\text{Cd}}$ ,  $V_{\text{La}}$ , and  $\text{Cd}_{\text{La}}$  form relatively shallow acceptor levels of  $\epsilon(0/-2)$ ,  $\epsilon(0/-1)$ , and  $\epsilon(0/-1)$  at 0.17, 0.26, and 0.15 eV from the VBM, respectively. Nevertheless, these defects are not considered to contribute significantly to hole generation because of their high formation energies. In addition, the formation energies of donor-type defects such as  $\text{Cd}_i$ ,  $V_{\text{Se}}$ , and  $V_{\text{O}}$  are quite low or even negative when the Fermi level is close to the VBM, even though they are maximized at the Anion-rich condition in terms of the chemical potential dependence. In particular, the formation energy of  $\text{Cd}_i^{+2}$  is negative when the Fermi level is below 0.59 eV, which indicates that the holes generated by the acceptor-type defects are strongly compensated by  $\text{Cd}_i^{+2}$ .

For  $\epsilon(0/-2)$  of  $V_{\text{Cd}}$ ,  $\epsilon(+2/0)$  of  $V_{\text{Se}}$ ,  $\epsilon(+2/0)$  of  $\text{Cd}_i$ , and  $\epsilon(0/-2)$  of  $\text{Se}_i$ , the defect charge states change discontinuously with unstable intermediate charge states (Fig. 3). This is due to the negative- $U$  effect,<sup>47</sup> which appears when the structure relaxation and chemical bonding around defects are significantly different between the relevant charge states.

In summary,  $V_{\text{Cd}}^{-2}$  and  $\text{Cd}_i^{+2}$  are dominant acceptor-type and donor-type native defects in  $\text{La}_2\text{CdO}_2\text{Se}_2$ , respectively. The balance of  $V_{\text{Cd}}^{-2}$  and  $\text{Cd}_i^{+2}$ , which are associated with Cd deficiency and excess, respectively, leads the equilibrium Fermi level to a mid-gap position in undoped  $\text{La}_2\text{CdO}_2\text{Se}_2$  at both the extreme conditions shown in Figs. 3(a) and 3(b). Therefore, undoped  $\text{La}_2\text{CdO}_2\text{Se}_2$  is expected to exhibit nearly stoichiometric and electrical insulating properties under any thermodynamical equilibrium growth conditions, in consistency with the experimental report on the stoichiometry and electrical properties of undoped samples.<sup>25</sup> In addition, even if extrinsic doping is attempted, carrier compensation due to the spontaneous formation of  $V_{\text{Cd}}^{-2}$  and  $\text{Cd}_i^{+2}$  would be inevitable, limiting the control of the Fermi level.

### 3.3 Donor and acceptor doping

Before the computationally demanding investigation of carrier doping in  $\text{La}_2\text{CdO}_2\text{Se}_2$  using the HSE06 hybrid functional, candidate dopants were screened using the Perdew-Burke-Ernzerhof functional tuned for solid within the generalized gradient approximation<sup>52</sup> with a Hubbard  $U$ <sup>53</sup> correction (PBEsol-GGA+ $U$ ). The effective  $U$  value of 5.0 eV was used for the Cd 4d-orbitals. The band edges were corrected by non-self-consistent HSE06 (nsc-HSE06) functional calculations on top of PBEsol-GGA+ $U$ , where non-self-consistency allows for direct band alignment between the PBEsol-GGA+ $U$  and hybrid functional results for the band-edge correction while maintaining reasonable computational accuracy compared to a conventional self-consistent approach.<sup>54,55</sup> The donor dopants assumed were  $\text{Ti}_{\text{La}}$ ,  $\text{Zr}_{\text{La}}$ ,  $\text{Hf}_{\text{La}}$ ,  $\text{Al}_{\text{Cd}}$ ,  $\text{Ga}_{\text{Cd}}$ , and  $\text{In}_{\text{Cd}}$ , and the acceptor dopants were  $\text{Mg}_{\text{La}}$ ,  $\text{Ca}_{\text{La}}$ ,  $\text{Sr}_{\text{La}}$ ,  $\text{Ba}_{\text{La}}$ ,  $\text{Li}_{\text{Cd}}$ ,  $\text{Na}_{\text{Cd}}$ ,  $\text{K}_{\text{Cd}}$ , and  $\text{Rb}_{\text{Cd}}$ . Only single acceptors/donors were taken into account. For donor dopants, we targeted Al and Zr, which have been employed in previous experiments,<sup>25</sup> and relevant elements in the same groups, Ga, In, Ti, and Hf. Because degenerate p-type conduction has been achieved by Mg doping in

LaCuOCh,<sup>17</sup> which has a similar crystal structure to La<sub>2</sub>CdO<sub>2</sub>Se<sub>2</sub>, Mg and group-II elements, namely Ca, Sr, and Ba, were considered as acceptor dopants for the La site. Group-I elements were employed as acceptor dopants for the Cd sites. Cu, Ag, and Au were not considered as they could form localized, deep states derived from their d-orbitals near the VBM. For all of the dopant elements, the interstitials (Ti<sub>i</sub>, Zr<sub>i</sub>, Hf<sub>i</sub>, Al<sub>i</sub>, Ga<sub>i</sub>, In<sub>i</sub>, Mg<sub>i</sub>, Ca<sub>i</sub>, Sr<sub>i</sub>, Ba<sub>i</sub>, Li<sub>i</sub>, Na<sub>i</sub>, K<sub>i</sub>, and Rb<sub>i</sub>) were also considered. The calculation conditions, the band-edge correction method, the formation energy diagrams for these dopants [Fig. S1], and the chemical potential conditions and competing phases [Tables S3-S16] are shown in the ESI†.

For the donor dopants, all of the above candidates form deep donor levels associated with localized states even at the PBEsol-GGA+*U* level [Fig. S1]. We selected Zr and Al as the best donor dopants, which have the shallowest donor levels at each cation site. In contrast, all of the acceptor dopants show shallow acceptor levels associated with hydrogenic effective-mass states [Fig. S1]. Sr and Na were selected as the most promising acceptor dopants in terms of the balance between the formation energies at the substitutional and interstitial sites, where the former and latter cases act as acceptors and donors, respectively.

To evaluate the formation energies of the selected dopants using the HSE06 functional, we calculated the chemical potential diagrams for the La-Cd-O-Se-X (X = Zr, Al, Sr, Na) quinary systems and found that the numbers of the chemical potential limits where La<sub>2</sub>CdO<sub>2</sub>Se<sub>2</sub> can exist in the single phase are sixteen for Al and twelve for the others (see the ESI† [Tables S17-20] for each chemical potential limit and competing phase). To discuss the formation energies of the dopants in the situation with the least carrier compensation by the native defects, the following limits are considered: (i) the limits where the chemical potentials of the dopants are maximized under the Cation-rich condition [ $\Delta\mu_{\text{Zr}} = -2.83$  and  $\Delta\mu_{\text{Al}} = -1.89$  (eV)] for Zr and Al and (ii) the limits where the chemical potentials of the dopants are maximized under the Anion-rich condition [ $\Delta\mu_{\text{Sr}} = -4.10$  and  $\Delta\mu_{\text{Na}} = -1.63$  (eV)] for Sr and Na. Hereafter, we will refer to the former as the Cation-rich condition and the latter as the Anion-rich condition.

Figure 4(a) shows the formation energies of the selected donor dopants (Zr<sub>La</sub>, Al<sub>Cd</sub>, Zr<sub>i</sub>, and Al<sub>i</sub>) in La<sub>2</sub>CdO<sub>2</sub>Se<sub>2</sub> at the Cation-rich condition along with those of the native defects. When the Fermi level is high, the formation energies of Zr<sub>La</sub> and Al<sub>Cd</sub> are considerably lower than those of Zr<sub>i</sub> and Al<sub>i</sub>. Although Zr<sub>La</sub> shows a relatively low formation energy, its donor level [ $\epsilon(+1/0)$ ] at  $-0.43$  eV from the CBM is not very shallow. Al<sub>Cd</sub> and Al<sub>i</sub> show negative-*U* behavior, where the neutral and +2 charge state is unstable, respectively. The resultant donor-to-acceptor transition level [ $\epsilon(+1/-1)$ ] of Al<sub>Cd</sub> is quite shallow at 0.03 eV from the CBM. However, since the formation energy is high when the Fermi level is close to the CBM, the solubility would prevent net carrier generation. Moreover, electron compensation due to the spontaneous formation of  $V_{\text{Cd}}^{-2}$  limits the increase in the Fermi level, as discussed in Sec. 3.2.

Figure 4(b) shows the formation energies of the selected substitutional acceptor dopants and the corresponding interstitials

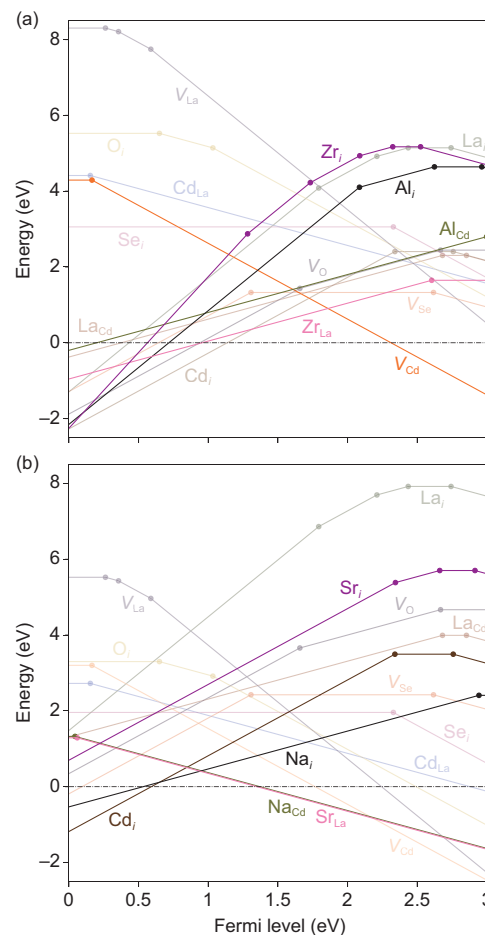


Fig. 4 (a) Formation energies of Zr and Al dopants and native defects in La<sub>2</sub>CdO<sub>2</sub>Se<sub>2</sub> at Cation-rich condition. (b) Formation energies of Sr and Na dopants and native defects in La<sub>2</sub>CdO<sub>2</sub>Se<sub>2</sub> at Anion-rich condition. The results are presented in the same manner as Fig. 3. The positions of the thermodynamic transition levels are listed in Table S2.

(Sr<sub>La</sub>, Na<sub>Cd</sub>, Sr<sub>i</sub>, and Na<sub>i</sub>) in La<sub>2</sub>CdO<sub>2</sub>Se<sub>2</sub> at the Anion-rich condition along with those of the native defects. For the Na dopant, Na<sub>Cd</sub> is energetically preferred when the Fermi level is above 0.95 eV, and Na<sub>i</sub> is preferred below 0.95 eV. The acceptor level of Na<sub>Cd</sub> [ $\epsilon(0/-1)$ ] is 0.04 eV from VBM, and the donor level of Na<sub>i</sub> [ $\epsilon(+1/0)$ ] is  $-0.09$  eV from the CBM, both of which are quite shallow. However, Na is not suitable for carrier doping since its substitution and interstitial act to compensate the generated carriers with each other. For the Sr dopant, Sr<sub>La</sub> is energetically favorable over a wide Fermi level range except that below 0.22 eV, and Sr<sub>i</sub> has a high formation energy over the entire Fermi level range. Since Sr<sub>La</sub> forms quite a shallow acceptor level of  $\epsilon(0/-1)$  at 0.06 eV from the VBM, it would contribute significantly to the hole generation. Nevertheless, the hole concentration is not expected to increase much because of the hole compensation by the spontaneous formation of  $\text{Cd}_i^{+2}$ , as discussed in Sec. 3.2.

In summary, our theoretical defect energetics supports the choice of Zr and Al donor dopants considered in Ref.<sup>25</sup> and attributes the unsuccessful n-type doping to the carrier compensation by the spontaneous formation of  $V_{\text{Cd}}^{-2}$ . Furthermore, it is difficult to make La<sub>2</sub>CdO<sub>2</sub>Se<sub>2</sub> p-type because of the hole compen-

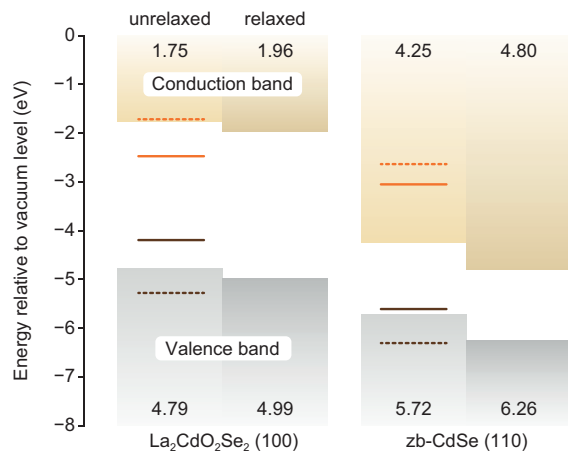


Fig. 5 Band-edge positions of  $\text{La}_2\text{CdO}_2\text{Se}_2$  (100) and  $\text{zb-CdSe}$  (110) surfaces with respect to the vacuum level. For each system, the results with unrelaxed and relaxed internal coordinates are shown on the left and right, respectively. The IP and EA values are indicated at the bottom and top of the figure, respectively. n-Type doping limits determined by the spontaneous formation of  $V_{\text{Cd}}^{-2}$  are shown as solid orange lines, and p-type doping limits determined by the spontaneous formation of  $\text{Cd}_i^{+2}$  are shown as solid brown lines. The doping limits without structure relaxation around defects are shown as dashed lines of the same colors. The chemical potential is set to the Cation-rich condition ( $\Delta\mu_{\text{Cd}} = 0$  eV) for the n-type doping limits and at the Anion-rich condition ( $\Delta\mu_{\text{Cd}} = -1.09$  eV) for the p-type doping limits.

sation by the spontaneous formation of  $\text{Cd}_i^{+2}$ , even though there is a suitable acceptor dopant like Sr that is easily soluble and forms a shallow acceptor level.

### 3.4 Doping limits

In Sec. 3.2, we explained that the spontaneous formation of  $V_{\text{Cd}}^{-2}$  and  $\text{Cd}_i^{+2}$  causes carrier compensation in  $\text{La}_2\text{CdO}_2\text{Se}_2$ , thereby limiting its carrier doping. In this section, we compare how the doping limits determined by  $V_{\text{Cd}}^{-2}$  and  $\text{Cd}_i^{+2}$  differ between  $\text{La}_2\text{CdO}_2\text{Se}_2$  and  $\text{zb-CdSe}$ , the local structures of which are similar to each other [Fig. 1]. The details of the defect calculations for  $\text{zb-CdSe}$  can be found in the ESI†.

Figure 5 shows the band edges of  $\text{La}_2\text{CdO}_2\text{Se}_2$  and  $\text{zb-CdSe}$ , the n-type doping limits (Fermi level upper limits) determined by the spontaneous formation of  $V_{\text{Cd}}^{-2}$  (i.e., the positive-to-negative transition of its formation energy), and the p-type doping limits (Fermi level lower limits) determined by  $\text{Cd}_i^{+2}$ . Here, the n-type doping limits at the Cation-rich condition ( $\Delta\mu_{\text{Cd}} = 0$  eV) and the p-type doping limits at the Anion-rich condition ( $\Delta\mu_{\text{Cd}} = -1.09$  eV) are considered, as these conditions provide the upper and lower limits of the Fermi level in terms of the chemical potential dependence, respectively. A previous study has proposed that the band-edge position is a good indicator of carrier dopability, with higher VBM facilitating hole doping and lower CBM facilitating electron doping.<sup>56–58</sup> In order to compare the band-edge positions between the different systems, the band alignment is performed using the vacuum level as a common reference. The positions of the VBM and CBM relative to the vacuum level, i.e., the negatives of the ionization potential (IP) and electron

affinity (EA), were determined using a method combining bulk and slab-vacuum models.<sup>48</sup> Slab-vacuum models of the nonpolar (100) surface of  $\text{La}_2\text{CdO}_2\text{Se}_2$  and the nonpolar (110) surface of  $\text{zb-CdSe}$  were constructed following the procedure described in Ref.<sup>59</sup>. In both models, the slab and vacuum thicknesses of more than 20 Å were ensured for sufficient potential convergence inside the slab and the vacuum region. The IPs and EAs were calculated in two cases with and without internal coordinate relaxation [Fig. 5]. The IP value for the relaxed  $\text{zb-CdSe}$  (110) surface is close to a previous estimate using the HSE06 functional and an experimental lattice parameter<sup>60</sup> and shows a reasonable agreement with a reported experimental IP value of 6.62 eV.<sup>61</sup> The relaxation of the internal coordinates shifts the band edges of  $\text{La}_2\text{CdO}_2\text{Se}_2$  and  $\text{zb-CdSe}$  downward by 0.20 eV and 0.54 eV, respectively. Since the structural relaxation considerably affects the IP and EA through the change in the surface dipoles,<sup>62,63</sup> we will discuss the doping limits based on the unrelaxed surfaces excluding such effects.

Comparing the band-edge positions of  $\text{La}_2\text{CdO}_2\text{Se}_2$  and  $\text{zb-CdSe}$ , the former is higher in both VBM and CBM than the latter, and the difference is more pronounced in the CBM [Fig. 5]. Therefore,  $\text{zb-CdSe}$  is much easier in electron doping and more difficult in hole doping than  $\text{La}_2\text{CdO}_2\text{Se}_2$ , according to the band alignment based consideration.<sup>56–58</sup> In fact, wurtzite- $\text{CdSe}$  is generally known as an n-type semiconductor,<sup>64</sup> but there is a report that  $\text{zb-CdSe}$  becomes a p-type semiconductor by N doping.<sup>65</sup> The n-type doping limit is slightly higher, while the p-type doping limit is significantly higher for  $\text{La}_2\text{CdO}_2\text{Se}_2$  than those for  $\text{zb-CdSe}$  [Fig. 5]. As discussed in Sec. 3.1, the orbital components forming the band edges of  $\text{La}_2\text{CdO}_2\text{Se}_2$  and  $\text{zb-CdSe}$  are similar, but the positions of the doping limits are not neatly aligned as in the case of the n-type doping limits determined by the  $V_{\text{Cu}}^{-1}$  in  $\text{CuMO}_2$ .<sup>29</sup> Given the similar local structures of  $\text{La}_2\text{CdO}_2\text{Se}_2$  and  $\text{zb-CdSe}$ , it was expected that the ease of the  $V_{\text{Cd}}^{-2}$  and  $\text{Cd}_i^{+2}$  formation would not differ much, but in fact, both defects are more easily formed in  $\text{La}_2\text{CdO}_2\text{Se}_2$  (see Fig. S2 in the ESI† for the formation energies of the  $V_{\text{Cd}}$  and  $\text{Cd}_i$  in  $\text{zb-CdSe}$ ). Such formation energy differences between  $\text{La}_2\text{CdO}_2\text{Se}_2$  and  $\text{zb-CdSe}$  are reflected in their doping limit differences in Fig. 5. To clarify this tendency, we analyzed the local structure of  $V_{\text{Cd}}^{-2}$  and  $\text{Cd}_i^{+2}$  before and after structure relaxation in each material [Fig. 6].

For  $V_{\text{Cd}}^{-2}$ , the change in the average distance due to the structure relaxation between the vacant Cd site and the four Se nearest neighbors is +0.15 Å for  $\text{La}_2\text{CdO}_2\text{Se}_2$  [Fig. 6(a)], whereas -0.18 Å for  $\text{zb-CdSe}$  [Fig. 6(b)]. For  $\text{Cd}_i^{+2}$ , the average distance to the four Se nearest neighbors is almost unchanged: -0.03 Å for  $\text{La}_2\text{CdO}_2\text{Se}_2$  [Fig. 6(c)] and -0.00 Å for  $\text{zb-CdSe}$  [Fig. 6(d)]. However, the change in the average distances to the four and six Cd neighbors is +0.36 and +0.19 Å for  $\text{La}_2\text{CdO}_2\text{Se}_2$  [Fig. 6(c)] and  $\text{zb-CdSe}$  [Fig. 6(d)], respectively. The larger outward relaxation in the former may be partly attributed to the 0.2 Å shorter original distance between the interstitial and Cd sites (See Fig. 6 caption). In contrast to  $\text{zb-CdSe}$ ,  $\text{La}_2\text{CdO}_2\text{Se}_2$  has four La at 4.04 Å from the interstitial Cd site, but their average distance change due to the relaxation is only +0.06 Å. Thus, although  $\text{La}_2\text{CdO}_2\text{Se}_2$  and  $\text{zb-CdSe}$  have similar local structures around

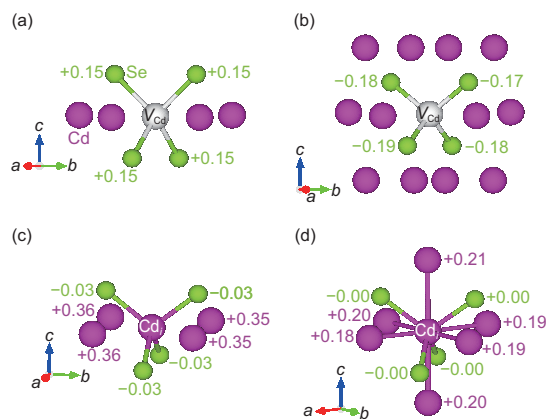


Fig. 6 Relaxed local structures of  $V_{\text{Cd}}^{-2}$  in (a)  $\text{La}_2\text{CdO}_2\text{Se}_2$  and (b)  $\text{zb-CdSe}$  and  $\text{Cd}_i^{+2}$  in (c)  $\text{La}_2\text{CdO}_2\text{Se}_2$  and (d)  $\text{zb-CdSe}$ . The changes in the distances from the vacancy or interstitial sites to the neighboring atoms by structural relaxation are shown in Å. The original distances before relaxation are (a) 2.68 Å, (b) 2.66 Å, (c) 2.68 Å to Se and 2.88 Å to Cd, and (d) 2.66 Å to Se and 3.08 Å to Cd.

$V_{\text{Cd}}^{-2}$  and  $\text{Cd}_i^{+2}$  before structure relaxation, noticeable differences are found in the amount of relaxation.

To quantitatively compare the effect of relaxation on the doping limits, we calculated the formation energies of  $V_{\text{Cd}}^{-2}$  and  $\text{Cd}_i^{+2}$  without structure relaxation and show the resultant doping limits in Fig. 5. The cell-size correction term for the formation energy without relaxation was calculated using only the ion-clamped dielectric tensor. The structure relaxation is found to lower the formation energies of  $V_{\text{Cd}}^{-2}$  and  $\text{Cd}_i^{+2}$  in  $\text{La}_2\text{CdO}_2\text{Se}_2$  more significantly than that in  $\text{zb-CdSe}$ , changing the doping limits accordingly. Especially for  $\text{Cd}_i^{+2}$  in  $\text{La}_2\text{CdO}_2\text{Se}_2$ , the change in the formation energy due to the structural relaxation is conspicuous, resulting in a large shift of the p-type doping limit upward by 1.09 eV. Judging comprehensively from the band-edge positions and the doping limits, the difference in the degree of electron compensation between the two materials is largely due to the difference in the CBM positions, while the difference in the degree of hole compensation is due to the difference in the  $\text{Cd}_i^{+2}$  formation energy.

## 4 Conclusions

We have theoretically investigated the bulk, native defect, and dopant properties of  $\text{La}_2\text{CdO}_2\text{Se}_2$  using the HSE06 hybrid functional. The calculated structural parameters and band gap are reasonably consistent with the reported experimental values. The DOS analysis indicates that the band gap of  $\text{La}_2\text{CdO}_2\text{Se}_2$  is mainly determined by the selenide layer since the VBM is formed mainly from Se p-orbitals and the CBM mainly from Cd s-orbitals. The band-averaged effective masses of both electron and hole exhibit anisotropy due to the layered structure, being lighter in the in-plane direction and heavier in the out-of-plane direction with a much larger anisotropy for the hole.

From the energetics of the native defects, we found that under any thermodynamic equilibrium conditions, the spontaneous formation of the acceptor-type  $V_{\text{Cd}}^{-2}$  defect occurs when the Fermi level is high, resulting in significant electron compensation. Sim-

ilarly, the spontaneous formation of the donor-type  $\text{Cd}_i^{+2}$  defect occurs when the Fermi level is low, resulting in severe hole compensation. The balance of  $V_{\text{Cd}}^{-2}$  and  $\text{Cd}_i^{+2}$  leads the equilibrium Fermi level to a mid-gap position in undoped  $\text{La}_2\text{CdO}_2\text{Se}_2$  without a substantial off-stoichiometry. The calculations of the selected Zr and Al dopants show that  $\text{Zr}_{\text{La}}$  has a low formation energy but a relatively deep donor level, and  $\text{Al}_{\text{Cd}}$  forms the  $\epsilon$  (+1/−1) level slightly below the CBM with a moderate formation energy. From the calculations of various dopants selected from group-I and II elements, it is suggested that  $\text{Sr}_{\text{La}}$  is the best acceptor dopant because it forms quite a shallow acceptor level with a low formation energy. In contrast, Na is not suitable for hole doping because it energetically prefers the donor-type  $\text{Na}_i$  form when the Fermi level is low, rather than the acceptor-type  $\text{Na}_{\text{Cd}}$  form. However, even with extrinsic doping, it is difficult to make  $\text{La}_2\text{CdO}_2\text{Se}_2$  n- and p-type because of the carrier compensation by  $V_{\text{Cd}}^{-2}$  and  $\text{Cd}_i^{+2}$ , respectively.

From the band alignment of  $\text{La}_2\text{CdO}_2\text{Se}_2$  and  $\text{zb-CdSe}$  with respect to the vacuum level, we found that the VBM is higher and the CBM is considerably higher in  $\text{La}_2\text{CdO}_2\text{Se}_2$  than those in  $\text{zb-CdSe}$ . The n-type doping limit determined by  $V_{\text{Cd}}^{-2}$  is slightly higher and the p-type doping limit determined by  $\text{Cd}_i^{+2}$  is significantly higher for  $\text{La}_2\text{CdO}_2\text{Se}_2$  than those for  $\text{zb-CdSe}$  in the vacuum-level-based band alignment. The substantial electron compensation in  $\text{La}_2\text{CdO}_2\text{Se}_2$  compared to  $\text{zb-CdSe}$  is attributed mainly to the much higher CBM position, while the severe hole compensation is largely due to the lower  $\text{Cd}_i^{+2}$  formation energy enhanced by the significant structural relaxation effects.

## Conflicts of interest

There are no conflicts to declare.

## Acknowledgements

This work was supported by JSPS KAKENHI Grant Numbers JP20J23137, JP20H00302, and JP21H04612, JST CREST Grant Number JPMJCR17J2, and Design and Engineering by Joint Inverse Innovation for Materials Architecture project from MEXT. The computing resources of Academic Center for Computing and Media Studies at Kyoto University, Research Institute for Information Technology at Kyushu University, and National Institute of Advanced Industrial Science and Technology were used for part of this work. The crystal structures in Fig. 1 and Fig. 6 were drawn using the VESTA code.<sup>66</sup>

## References

- 1 *Transparent Electronics: From Synthesis to Applications*, ed. A. Facchetti and T. Marks, Wiley, New York, 2010.
- 2 S. C. Dixon, D. O. Scanlon, C. J. Carmalt and I. P. Parkin, *J. Mater. Chem. C*, 2016, **4**, 6946–6961.
- 3 I. Hamberg and C. G. Granqvist, *J. Appl. Phys.*, 1986, **60**, R123–R160.
- 4 N. Taga, H. Odaka, Y. Shigesato, I. Yasui, M. Kamei and T. E. Haynes, *J. Appl. Phys.*, 1996, **80**, 978–984.
- 5 H. Ohta, M. Orita, M. Hirano, H. Tanji, H. Kawazoe and H. Hosono, *Appl. Phys. Lett.*, 2000, **76**, 2740–2742.

- 6 H. Randhawa, M. Matthews and R. Bunshah, *Thin Solid Films*, 1981, **83**, 267–271.
- 7 R. Banerjee and D. Das, *Thin Solid Films*, 1987, **149**, 291–301.
- 8 T. Ishida, O. Tabata, J. il Park, S. H. Shin, H. Magara, S. Tamura, S. Mochizuki and T. Mihara, *Thin Solid Films*, 1996, **281-282**, 228–231.
- 9 T. Minami, H. Nanto and S. Takata, *Appl. Phys. Lett.*, 1982, **41**, 958–960.
- 10 T. Minami, H. Sato, H. Nanto and S. Takata, *Jpn. J. Appl. Phys.*, 1985, **24**, L781–L784.
- 11 H. Kawazoe, M. Yasukawa, H. Hyodo, M. Kurita, H. Yanagi and H. Hosono, *Nature*, 1997, **389**, 939–942.
- 12 K. Ueda, T. Hase, H. Yanagi, H. Kawazoe, H. Hosono, H. Ohta, M. Orita and M. Hirano, *J. Appl. Phys.*, 2001, **89**, 1790–1793.
- 13 H. Yanagi, T. Hase, S. Ibuki, K. Ueda and H. Hosono, *Appl. Phys. Lett.*, 2001, **78**, 1583–1585.
- 14 A. Kudo, H. Yanagi, H. Hosono and H. Kawazoe, *Appl. Phys. Lett.*, 1998, **73**, 220–222.
- 15 A. Bhatia, G. Hautier, T. Nilgianskul, A. Miglio, J. Sun, H. J. Kim, K. H. Kim, S. Chen, G.-M. Rignanese, X. Gonze and J. Suntivich, *Chem. Mater.*, 2016, **28**, 30–34.
- 16 K. Ueda, S. Inoue, S. Hirose, H. Kawazoe and H. Hosono, *Appl. Phys. Lett.*, 2000, **77**, 2701–2703.
- 17 H. Hiramatsu, K. Ueda, H. Ohta, M. Hirano, T. Kamiya and H. Hosono, *Appl. Phys. Lett.*, 2003, **82**, 1048–1050.
- 18 H. Hiramatsu, K. Ueda, H. Ohta, M. Hirano, M. Kikuchi, H. Yanagi, T. Kamiya and H. Hideo, *Appl. Phys. Lett.*, 2007, **91**, 012104.
- 19 K. H. L. Zhang, K. Xi, M. G. Blamire and R. G. Egdell, *J. Phys.: Condens. Matter*, 2016, **28**, 383002.
- 20 J. Willis and D. O. Scanlon, *J. Mater. Chem. C*, 2021, **9**, 11995–12009.
- 21 H. Hiramatsu, H. Kamioka, K. Ueda, H. Ohta, T. Kamiya, M. Hirano and H. Hosono, *Phys. Status Solidi A*, 2006, **203**, 2800–2811.
- 22 K. Ueda and H. Hosono, *J. Appl. Phys.*, 2002, **91**, 4768–4770.
- 23 K. Ueda, H. Hiramatsu, H. Ohta, M. Hirano, T. Kamiya and H. Hosono, *Phys. Rev. B*, 2004, **69**, 155305.
- 24 D. O. Scanlon, J. Buckeridge, C. R. A. Catlow and G. W. Watson, *J. Mater. Chem. C*, 2014, **2**, 3429–3438.
- 25 H. Hiramatsu, K. Ueda, T. Kamiya, H. Ohta, M. Hirano and H. Hosono, *J. Mater. Chem.*, 2004, **14**, 2946–2950.
- 26 H. Hiramatsu, K. Ueda, T. Kamiya, H. Ohta, M. Hirano and H. Hosono, *J. Phys. Chem. B*, 2004, **108**, 17344–17351.
- 27 D. O. Scanlon, B. J. Morgan, G. W. Watson and A. Walsh, *Phys. Rev. Lett.*, 2009, **103**, 096405.
- 28 D. O. Scanlon and G. W. Watson, *J. Phys. Chem. Lett.*, 2010, **1**, 3195–3199.
- 29 T. Gake, Y. Kumagai, A. Takahashi and F. Oba, *Phys. Rev. Materials*, 2021, **5**, 104602.
- 30 G. Hautier, A. Miglio, G. Ceder, G.-M. Rignanese and X. Gonze, *Nat. Commun.*, 2013, **4**, 2292.
- 31 X. Cai and S.-H. Wei, *Appl. Phys. Lett.*, 2021, **119**, 070502.
- 32 P. E. Blöchl, *Phys. Rev. B*, 1994, **50**, 17953–17979.
- 33 J. Paier, M. Marsman, K. Hummer, G. Kresse, I. C. Gerber and J. G. Ángyán, *J. Chem. Phys.*, 2006, **124**, 154709.
- 34 G. Kresse and J. Furthmüller, *Phys. Rev. B*, 1996, **54**, 11169–11186.
- 35 G. Kresse and D. Joubert, *Phys. Rev. B*, 1999, **59**, 1758–1775.
- 36 J. Heyd, G. E. Scuseria and M. Ernzerhof, *J. Chem. Phys.*, 2003, **118**, 8207–8215.
- 37 A. V. Krugau, O. A. Vydrov, A. F. Izmaylov and G. E. Scuseria, *J. Chem. Phys.*, 2006, **125**, 224106.
- 38 Y. Hinuma, G. Pizzi, Y. Kumagai, F. Oba and I. Tanaka, *Comput. Mater. Sci.*, 2017, **128**, 140–184.
- 39 A. Togo and I. Tanaka, 2018, arXiv:1808.01590.
- 40 G. K. Madsen, J. Carrete and M. J. Verstraete, *Comput. Phys. Commun.*, 2018, **231**, 140–145.
- 41 Y. Kumagai, N. Tsunoda, A. Takahashi and F. Oba, *Phys. Rev. Materials*, 2021, **5**, 123803.
- 42 S. P. Ong, W. D. Richards, A. Jain, G. Hautier, M. Kocher, S. Cholia, D. Gunter, V. L. Chevrier, K. A. Persson and G. Ceder, *Comput. Mater. Sci.*, 2013, **68**, 314–319.
- 43 C. Freysoldt, J. Neugebauer and C. G. Van de Walle, *Phys. Rev. Lett.*, 2009, **102**, 016402.
- 44 Y. Kumagai and F. Oba, *Phys. Rev. B*, 2014, **89**, 195205.
- 45 A. Jain, S. P. Ong, G. Hautier, W. Chen, W. D. Richards, S. Dacek, S. Cholia, D. Gunter, D. Skinner, G. Ceder and K. A. Persson, *APL Mater.*, 2013, **1**, 011002.
- 46 R. W. Nunes and X. Gonze, *Phys. Rev. B*, 2001, **63**, 155107.
- 47 C. Freysoldt, B. Grabowski, T. Hickel, J. Neugebauer, G. Kresse, A. Janotti and C. G. Van de Walle, *Rev. Mod. Phys.*, 2014, **86**, 253–305.
- 48 F. Oba and Y. Kumagai, *Appl. Phys. Express*, 2018, **11**, 060101.
- 49 K. Ueda and H. Hosono, *Thin Solid Films*, 2002, **411**, 115–118.
- 50 N. Samarth, H. Luo, J. K. Furdyna, S. B. Qadri, Y. R. Lee, A. K. Ramdas and N. Otsuka, *Appl. Phys. Lett.*, 1989, **54**, 2680–2682.
- 51 F. Ricci, W. Chen, U. Aydemir, G. J. Snyder, G.-M. Rignanese, A. Jain and G. Hautier, *Sci. Data*, 2017, **4**, 170085.
- 52 J. P. Perdew, A. Ruzsinszky, G. I. Csonka, O. A. Vydrov, G. E. Scuseria, L. A. Constantin, X. Zhou and K. Burke, *Phys. Rev. Lett.*, 2008, **100**, 136406.
- 53 V. I. Anisimov, J. Zaanen and O. K. Andersen, *Phys. Rev. B*, 1991, **44**, 943–954.
- 54 F. Tran, *Phys. Lett. A*, 2012, **376**, 879–882.
- 55 Y. Hinuma, Y. Kumagai, I. Tanaka and F. Oba, *Phys. Rev. B*, 2017, **95**, 075302.
- 56 H. Hosono, in *Transparent Electronics: From Synthesis to Applications*, Wiley, New York, 2010, ch. 2.
- 57 S. B. Zhang, S.-H. Wei and A. Zunger, *J. Appl. Phys.*, 1998, **83**, 3192–3196.
- 58 S. B. Zhang, S.-H. Wei and A. Zunger, *Phys. Rev. Lett.*, 2000, **84**, 1232–1235.
- 59 Y. Hinuma, Y. Kumagai, F. Oba and I. Tanaka, *Comput. Mater. Sci.*, 2016, **113**, 221–230.

- 60 A. Grüneis, G. Kresse, Y. Hinuma and F. Oba, *Phys. Rev. Lett.*, 2014, **112**, 096401.
- 61 *Semiconductor Surfaces and Interfaces*, ed. W. Mönch, Springer Berlin, Heidelberg, 2001.
- 62 Y. Hinuma, Y. Kumagai, I. Tanaka and F. Oba, *Phys. Rev. Materials*, 2018, **2**, 124603.
- 63 Y. Hinuma, T. Gake and F. Oba, *Phys. Rev. Materials*, 2019, **3**, 084605.
- 64 L. Zhao, L. Hu and X. Fang, *Adv. Funct. Mater.*, 2012, **22**, 1551–1566.
- 65 T. Ohtsuka, J. Kawamata, Z. Zhu and T. Yao, *Appl. Phys. Lett.*, 1994, **65**, 466–468.
- 66 K. Momma and F. Izumi, *J. Appl. Crystallogr.*, 2011, **44**, 1272–1276.